
EFDA–JET–PR(05)46

M.E. Puiatti, M. Valisa, C. Angioni, L. Garzotti, P. Mantica, M. Mattioli,
L. Carraro, I. Coffey, C. Sozzi and JET EFDA contributors

Analysis of Metallic Impurity Density Profiles in Low Collisionality JET H-Mode and L-Mode Plasmas

“This document is intended for publication in the open literature. It is made available on the understanding that it may not be further circulated and extracts or references may not be published prior to publication of the original when applicable, or without the consent of the Publications Officer, EFDA, Culham Science Centre, Abingdon, Oxon, OX14 3DB, UK.”

“Enquiries about Copyright and reproduction should be addressed to the Publications Officer, EFDA, Culham Science Centre, Abingdon, Oxon, OX14 3DB, UK.”

Analysis of Metallic Impurity Density Profiles in Low Collisionality JET H-Mode and L-Mode Plasmas

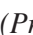
M.E. Puiatti¹, M. Valisa¹, C. Angioni², L. Garzotti¹, P. Mantica³, M. Mattioli¹,
L. Carraro¹, I.Coffey⁴, C. Sozzi³ and JET EFDA contributors*

¹*Consorzio RFX - Associazione Euratom-Enea sulla Fusione, I-35127 Padova, Italy*

²*Max Planck Institut für Plasmaphysik, EURATOM-IPP Association, D-85748 Garching, Germany*

³*IFP- Istituto di Fisica del Plasma- CNR-EURATOM, 20125 Milano, Italy*

⁴*Department of Physics, Queen's University, Belfast, UK*

* See annex of J. Pamela et al, "Overview of JET Results",
(Proc.  IAEA Fusion Energy Conference, Vilamoura, Portugal (2004)).

ABSTRACT

This paper describes the behaviour of nickel in L-mode and H-mode JET discharges characterized by the application of radiofrequency power heating and featuring ITER relevant collisionality. The impurity transport is analysed on the base of perturbative experiments (Laser Blow Off injection) and is compared with electron heat and deuterium transport. In the JET plasmas here analysed ICRH heating is applied either in Mode Conversion (MC) to heat the electrons or in Minority Heating (MH) to heat the ions. The two heating schemes have systematically different effects on nickel transport, yielding flat or slightly hollow nickel density profiles in the case of ICRH in MC and peaked nickel density profiles in the case of RF applied in MH. Accordingly, both diffusion coefficients and pinch velocities of nickel are found to be systematically different. Linear gyrokinetic calculations by means of the code GS2 provide a possible explanation of such different behaviour by exploring the effects produced by the different microinstabilities present in these plasmas. In particular trapped electron modes driven by the stronger electron temperature gradients measured in the MC cases, although subdominant, produce a contribution to the impurity pinch directed outwards that is qualitatively in agreement with the pinch reversal found in the experiment. Particles and heat diffusivities appear to be decoupled in MH shots, with χ_e and $D_D \gg D_{Ni}$, and are instead quite similar in the MC ones. In the latter case, nickel transport appears to be driven by the same turbulence that drives the electron heat transport and is sensitive to the value of the electron temperature gradient length. These findings give ground to the idea that in ITER it should be possible to find conditions in which the risk of accumulation of metals such as nickel can be contained.

1. INTRODUCTION

Understanding the impurity behaviour is a critical issue in the determination of a reactor performance. Impurities in the plasma core enhance radiation losses and plasma dilution with deleterious consequences on fusion reactivity. In particular, high Z impurity accumulation, with the associated risk of plasma disruption, cannot be tolerated. Therefore, in the ITER perspective, a critical point is to understand the behaviour of heavy impurity density profiles, if in any plasma condition accumulation is to be expected and what are the proper tools to control it.

Both experimental and theoretical understanding of the way the impurities behave in present day devices is relatively poor and does not allow an extrapolation to a reactor like condition. Experiments and studies regarding impurities have been certainly much more fragmented, for instance, than those concerning the behaviour of electrons and fuel particles, to which impurities are, by the way, inherently linked. The literature regarding the dependence of the electron density profile on the various regimes is in fact relatively abundant. Among the main results, the electron density peaking is known to scale inversely with collisionality [1-3] while the application of radio frequency heating has instead a flattening effect and the pump out induced in that way is more pronounced when heating is delivered through the electron channel [4-7]. An explanatory picture of such findings has also been attempted in the framework of the Ion Temperature Gradient modes (ITG) and Trapped Electron Modes (TEM) microinstabilities [1, 3, 8, 9, 10].

How the shape of the impurity profiles is related to the collisionality level, what are the dominant instabilities that determine the anomalous, i.e. non-ballistic, transport and the role of impurity charge is substantially unknown. One evidence that is common to various experiments is that central Radio-Frequency (RF) heating appears to be effective in flattening also the impurity profiles [11-18]. In particular, in ASDEX Upgrade it has been observed on the one hand the importance of the RF power deposition radius, and on the other hand that dominant electron heating via ECRH decontaminates the plasma core more efficiently than dominant ion heating via ICRH [12]. In DIII D [13] the flattening effect of ECRH on the electron density has been found to be effective also on the intrinsic nickel. In C-Mod [15], where a robust method for producing plasmas with Internal Transport Barriers (ITB) has been by off-axis ICRF heating, with only off-axis heating the plasma density continues to peak and impurities build up, leading to a radiative collapse. However, the addition of on-axis heating can arrest the density peaking as well as the impurity accumulation [19]. In JT-60U [14] ECRH heating has been able to flatten both electron and Ar densities in ITB's obtained in high β_p plasmas but not in the cases of reversed shear plasmas. In JET argon seeded discharges at high electron density the addition of ICRH to Neutral Beam Heating (NB) allows the avoidance of Ar central accumulation [16, 17]. In TCV an ECRH power scan in electron heating dominated discharges has shown that the confinement time of injected silicon reduces with power, with a large outward edge convective velocity [18].

This paper describes the analysis of the nickel behaviour following Laser Blow Off injection in L-mode and H-mode JET discharges characterized by the presence of radiofrequency power heating and featuring ITER relevant collisionality levels. In the discharges here examined the ICRH heating was applied according to two different schemes: either with $\sim 20\%$ ^3He concentration to obtain Mode Conversion (MC) and directly heat the electrons [20] or with $\sim 8\%$ ^3He to heat thermal ions according to the Minority Heating (MH) scheme. The effect of the two schemes on nickel was systematically different: nickel peaked in the case of RF heating in MH and showed instead slightly hollow or essentially flat profiles in the case of RF in MC.

Such different behavior, that can be ascribed either to the different RF heating channel (electrons or ions) and/or to the electron power deposition profiles, is discussed and compared with the behavior of the main gas particle profiles. Subsequently the experimental evidence is considered in the light of the assumption that the main instabilities thought to drive the anomalous heat transport are also responsible for both main particle and impurity transport, in the framework of the theory of TEM and ITG modes. This is done by evaluating the transport induced by ITG and TEM modes in cases with plasma parameters similar to the experimental ones. The linear version of the gyro-kinetic code GS2 [21] has been applied in order to identify the instabilities at play in these plasmas and compute the transport of a nickel impurity by means of a quasi-linear model. The latter, recently proposed, has been found to be in satisfactory agreement with non-linear gyrokinetic simulations [9].

In the described experiments the RF power was modulated for the purpose of characterizing the electron heat transport via the analysis of the heat pulse propagation [22,23]. This offered the opportunity

to compare the transport of nickel particles to the heat transport in the same discharges. Such comparison is of interest when projected to the reactor case, where particle transport should be fast to avoid impurity and alpha particle accumulation while heat transport should be low to increase the overall efficiency.

2. EXPERIMENTAL SET-UP AND ANALYSIS TOOLS

The experiments analyzed in the following include H-mode and L-mode plasma discharges.

Four discharges in H-mode ($B_t=3.28$ and $I_p= 1.8\text{MA}$) with ~ 3 MW of ICRH added on top of ~ 12 - 14MW of NB power have been analyzed in detail. In two shots (Pulse No's: 58149 and 58143) ICRH has been applied in MC to heat electrons (deposition radius $\rho = 0.37$, $\sim 20\%$ ^3He), in the other two (Pulse No's: 58142 and 58144) ICRH was centrally applied in MH with $\sim 8\%$ ^3He to heat thermal ions (deposition radius $\rho = 0.1$). These discharges are at low collisionality, $0.1 \leq \nu_{\text{eff}} \cdot d \leq 0.2$ at $\rho = 0.5$, where ν_{eff} is estimated as

$$\nu_{\text{eff}} = 10^{-14} \cdot n_e \cdot T_e^{-2} \cdot Z_{\text{eff}} \cdot R$$

with n_e in m^{-3} , T_e in eV, R major radius in m.

The time evolution of the main parameters of two H-mode shots, one with ICRH in MC and one in MH, is shown in fig.1a, b. The main heating is provided by 14 MW of NBI, with 3 MW of ICRH on top. The ICR wave is modulated up to 49.5 s to allow the determination of the turbulent heat diffusivity; the modulation is then switched off to perform the LBO and shallow pellets experiments without temperature perturbations.

Several L-mode discharges ($B_t = 3.25$ - 3.45 T and $I_p = 1.6$ - 1.85MA) with ~ 3.5 MW of ICRH in MC added on top of up to 9MW of NB power have also been analyzed.

In Fig.1 the SXR time traces show that in the H-mode discharges a relevant sawtooth activity (ST) is avoided by an on axis q value maintained above 1. If present, sawteeth have to be taken into account in the evaluation of the impurity transport parameters which are perturbed at crashes [16,17]. Actually, the L-mode shots feature significant ST. In particular, all the LBO pulses made in MH L-mode discharges were perturbed by ST, so that Ni behavior has been fully analyzed only in the MC discharges in L-mode.

Perturbative techniques have been used to evaluate the transport parameters. The ICRH modulation allows the determination of the turbulent electron heat diffusivity χ_e [22] in the discharges where the radiofrequency power was applied in MC.

The experimental tool used to analyze the Ni behavior was a Laser Blow-Off (LBO) pulse, marked with a vertical line in fig.1 at $t \sim 50\text{s}$ in the time traces of the radiated power and Soft X-Rays (SXR) brightness. The electron temperature drop and electron density increase at $t = 50.5$ in the MC shot is due to the presence of a shallow pellet, injected with the aim of determining the main particle transport coefficients [24]. Transient experiments such as LBO or shallow pellet are necessary to characterize

the particle transport, as they allow the discrimination between the diffusive and the convective term of the fluxes, i.e. the diffusion coefficient D and the pinch velocity v :

$$\Gamma_z = -D \cdot \frac{\delta n_z}{\delta r} + n \cdot v_z$$

where positive v corresponds to an outward pinch. On the contrary, from a steady state transport analysis, for both impurities and deuterium, only the peaking factor v/D can be determined. In the analysis of transient experiments such as LBO the usual question arises if the pulse itself is a cause of perturbation for the impurity transport, thus leading to the determination of diffusion coefficients and pinch velocities that are not representative of the steady state. In the transport simulations reported in this paper, D and v do not need to be changed throughout the LBO pulse to allow a good reconstruction of the experimental radiation pattern. Moreover, the extrapolation to the steady state made with the same D and v determined by means of the LBO analysis is well compatible with the data outside the laser pulse, as will be shown later. Therefore we conclude that the transport parameters deduced by means of the LBO pulses analyzed in this paper are also representative of the steady state.

The analysis of Ni behaviour has been performed by means of a 1D Collisional-Radiative (CR) impurity transport model [25] that simulates available Ni spectroscopic lines, inverted soft-X-ray brightness and bolometer data. The nickel atomic data used in the model are those detailed in [26]. The neoclassical transport of Ni has been calculated by means of NCLASS [27]. The transport parameters of deuterium have been analysed by means of the JETTO transport code [24]. To correlate the experimentally deduced transport parameters with the underlying instabilities the results of the H-mode discharges have been interpreted by the linear gyrokinetic code GS2 [21], where a trace of Nickel in extremely low concentration in order to be negligible in the quasi-neutrality condition has been added to the two main species, deuterium ions and electrons respectively.

3. RESULTS

3.1 H-MODE

As previously mentioned, the main difference between the two couples of H-mode discharges analyzed in this paper is the adopted RF heating scheme, which results in different total electron heating power deposition profiles, as shown in Fig.2(a). The contribution from NBI to the power deposition has been calculated by the PENCIL code [28], while RF deposition is obtained from PION [29] in the MH cases, and can only be extrapolated experimentally from the analysis of the modulation data in the MC cases [22]. RF power is mainly deposited directly to electron and off-axis in the MC discharges, e.g. Fig.2(a) shows that a peak appears around $\rho = 0.35$, whilst it is mainly deposited on-axis and to thermal ions via ^3He fast ions in the MH discharges. No difference is seen in the ion power deposition profiles (Fig.2(b)), whereas the effect of NBI is dominant. The electron and ion temperature profiles corresponding to one discharge with ICRH in MC (Pulse No: 58149) and one with ICRH in MH (Pulse No: 58144) are shown in Fig.3. The electron temperature (T_e) profile is obtained as an average between Thomson scattering and Electron Cyclotron Emission (ECE) measurements: the

two diagnostic systems give in these shots very similar profiles. The profiles shown in Fig.3 are 0.5s averages around the LBO time. In spite of the peaked electron power deposition profile, the MH discharges do not show higher on-axis electron temperatures and the electron temperature gradient is lower for $\rho < 0.5$.

The electron density profiles considered in this paper are obtained as Single Value Decomposition inversions of the interferometer data (Fig.4). The MH shots are characterized by lower values of both the density and the density gradient.

The radiation pattern observed in the plasma core in discharges with ICRH in MC or in MH is soundly different: in the MH discharges the injected Nickel remains in the centre for a longer time with much more peaked profiles than in the other case. Figures 5(a), (b) show the time evolution of Ni XXV (118 \approx) and of Ni XXVII (1.6 \approx) lines respectively in the four analysed shots ($t = 0$ corresponds to the time of the LBO pulse). While the behaviour of the Ni XXV line is basically the same in the four discharges, Ni XXVII shows a slower decay time in MH shots. Ni XXVII is a He-like ion, with a ionisation potential of 10.29keV and therefore emits from the plasma centre, while the lines from Ni XXV (ionisation potential 2.28keV) come from a more external region. This indicates that the Ni confinement time in the plasma centre in the MH discharges is longer than in the pulses with ICRH in MC. The different nickel central confinement is clearly shown also by SXR emissivities: the contour plots of the SXR inverted emissivities during the LBO pulses for the four discharges are reported in Fig.6, where the emissivities just before the laser pulse have been subtracted. The picture shows that for the MH case the penetration is slower and very peaked emissivity profiles remain in the plasma core for longer times.

Finally, the total radiated power due to LBO has a very similar time evolution in all these discharges, confirming that in terms of total radiated power the LBO contribution is essentially from the outer half of the plasma.

3.2 L-MODE

As an example, Fig.7 shows the electron temperature and electron power deposition profiles in two L-mode MC discharges. The main observation is that one discharge (Pulse No: 55802) features RF electron heating in the core ($\rho_{ICRH} = 0.13$) with an electron temperature gradient above the critical threshold for turbulence for $\rho > 0.1$, while in the other discharge (Pulse No: 55809) the electron heat deposition is more external ($\rho_{ICRH} = 0.32$) and the temperature gradient is above the threshold for turbulence for $\rho > 0.3$ [30]. The corresponding contour plot of the inverted SXR emissivities is shown in fig.8: Ni penetrates faster in Pulse No: 55802 and the penetration speed in both cases slows down where the electron temperature critical gradient is crossed [22, 23]. It has to be observed that during the LBO decay phase Pulse No: 55802 features a sawtooth, which perturbs the transport: the analysis reported in the next section will be limited to the time range before the sawtooth.

As already mentioned, the simulation has been made only for MC discharges, because no LBO pulse useful for a simulation has been done in similar L-mode MH discharges. However, the comparison

of unperturbed SXR emissivities (i.e. outside LBO for Pulse No: 55802) shows (Fig.9) that also in L-mode the profiles are more peaked when ICRH is applied in MH.

4. SIMULATIONS OF THE SPECTROSCOPIC DATA

In the 1-D CR impurity transport code used for the simulations, the diffusion coefficient and pinch velocity in the flux equation are free parameters, to be varied until a satisfactory reproduction of the radiation pattern is obtained. As the boundary condition the time behaviour of the Ni XVIII 118 \approx emission line is tracked. Independently of the transport parameters used for the calculation, the emissivity profile of this line is centred around $\rho \sim 0.9$, as will be shown in a following figure. This is just the region at which an edge transport barrier for impurities is usually found (and described here as a strong decrease of the diffusion coefficient). Therefore choosing the influx representative of the LBO pulse in such a way as to track the Ni XVIII line means that the edge transport coefficients are not determined; therefore the results discussed below refer to $\rho \leq 0.8$. The temporal profiles for the influxes used in the simulations to track the Ni XVIII line are triangular with a half maximum width of 2-3ms.

In order to avoid the subjectivity of the process, a minimisation procedure has been adopted in the reconstruction of Ni spectral lines from different ionisation states and of the SXR profiles at different times, aiming to converge to the best choice of transport parameters. For each run, four values of the radius are fixed (nodes), and it is assumed that D and the normalized pinch velocity ($v \cdot a/r$) are linear functions between two consecutive nodes. The values of D and v at the nodes are the parameters to be varied in order to minimise the difference between the experimental and calculated SXR profiles and SXR and Ni XXV brightnesses. This minimisation procedure is then repeated with different nodes. Procedures based on the same principle have been adopted to simulate different experiments as described for example in [12].

In this section, the experimental data are compared with the results corresponding to the best simulation.

In H-mode, the D and v profiles obtained for the two MH shots on the one hand and for the two MC shots on the other are basically the same, therefore one MH shot will be compared with one MC in the following. Figure 10 reports the best reconstruction of the time evolution of the Ni XXV and Ni XXVII spectral lines (already shown in Fig.5) and of the SXR brightness, while Fig.11 shows for the two discharges (one with ICRH in MH and the other one with ICRH in MC) the reconstruction of the inverted SXR profiles at three times during the LBO phase, corresponding respectively to the penetration phase, the phase around the maximum emission and the decay phase (the times are marked as dashed vertical lines in Fig.10). The corresponding normalized ion density profiles are shown in Fig.12: the shapes of the profiles are quite different, but in both cases Ni XVIII, chosen as the boundary condition for the influx, is populated at $\rho > 0.8$, while Ni XXVII (He-like) is the most populated ion located close to the axis. Ni XXV, also used for the reconstruction, emits around the mid-radius region characterised by the largest temperature and density gradients.

The transport parameters allowing the best reconstruction of the experimental radiation pattern have

been used for an extrapolation to a steady state, produced in the calculation with a constant Ni influx. The aim was to compare the steady state Ni density profiles in the two cases (Fig.13): in the MC shot the Ni density is slightly hollow throughout the radius, while the MH case features a strong on-axis peaking, with an higher Ni concentration in the centre (the Ni influx is the same).

Regarding the L-mode discharges, Fig.14 shows the simulation of the SXR brightness due to the injected Ni in the two shots considered here: the faster penetration of Ni in the discharge with the electron temperature gradient everywhere above the critical threshold for turbulence is clear.

In the simulations of both H-mode and L-mode, the SXR profiles obtained from the code at the steady state are well compatible with the experimental ones just before LBO (Fig.15 for H-mode). However, as the absolute value of Ni density was not available, to do this comparison the contribution from carbon and deuterium has been calculated and subtracted to the experimental SXR emissivity, assuming that all the remaining emission is from intrinsic nickel. Within this assumption, the result shown in Fig.15 supports the assertion that the diffusion coefficient and pinch velocity profiles determined by the LBO simulations are not perturbed values and are therefore representative of the steady state as well.

The diffusivities and pinch velocities necessary to reproduce the different brightness and SXR profile evolutions in the two H-mode discharges are shown in Fig.16, where they are also compared with the neoclassical values as obtained by the code NCLASS [27]. Instead of a single curve, for Ni D and v a stripe is shown, drawn by reporting at each radius the minimum and maximum values of D and v obtained as the best simulation in the various minimisation runs done with different nodes. The diffusion coefficient in the MH shot is characterised by a central region ($\rho \leq 0.2$) where its value is very low ($< 0.01 \text{ m}^2/\text{s}$), of the same order than the neoclassical D_{ncl} , while in the MC shot the diffusion coefficient is more than one order of magnitude higher than the neoclassical everywhere, in particular also in the central region. An important difference between the two shots is also obtained for the pinch velocity, that is inwards and of the order of 3-4 m/s at the mid radius in the MH shot, while is slightly outwards or close to zero for the MC discharge. For both shots the highest values of v and therefore the greatest difference between the two cases are found at intermediate radii, around $\rho \sim 0.3-0.5$.

In L-mode, (Fig.17), a central region of low diffusivity is found, as in H-mode. The pinch velocity results to be always inward in both cases, even if in Pulse No: 55809 its value is vary small in the portion of the radius below the threshold for turbulence in the temperature gradient. In L-mode, Ni transport is always highly anomalous: the diffusion coefficient exceeds the neoclassical value by more than one order of magnitude throughout the radius. The pinch velocity is about zero for discharge Pulse No: 55809 in the central region where the T_e gradient is below the turbulence threshold. However, differently from what found in H-mode for MC discharges, the pinch is in any case inward for $\rho \geq 0.3$, thus leading in L-mode to peaked Ni profiles also when ICRH is applied in MC.

5. COMPARISON WITH DEUTERIUM AND HEAT DIFFUSIVITIES

For the MC discharges, time dependent experiments have also been done to deduce the deuterium

particle diffusivity D_D (injection of a shallow pellet) [24] and the electron heat diffusivity χ_e (modulation of ICRH) [22]. Indeed, in the study of the impurity accumulation problem a figure of merit is the ratio of the transport parameters of the impurities to those of main fuel and electron thermal energy. In the published literature D_{imp}/χ_e , or more often $\tau_{\text{imp}}/\tau_{Ee}$, is reported to vary widely, depending on a variety of parameters such as elongation, triangularity, q_{95} . In Fig.18 the Ni diffusion coefficient corresponding to the minimum difference between simulation and experiment is compared with the deuterium and the heat diffusivities for the H-mode MC case (D_D, χ_e). The deuterium diffusion coefficient, determined by the reconstruction of the density profile evolution by means of the JETTO code, is substantially of the same order of the Ni one. It has to be mentioned that in the MH discharges, in absence of shallow pellet injections, the determination of D_D and v_D is not fully independent, but despite this uncertainty for $\rho \leq 0.2$ a deuterium diffusivity $D_D \gg D_{Ni}$ is necessary to reconstruct the electron density profiles given by the SVD inversions of the interferometer data.

As far as the heat diffusivity is concerned, fig. 18 shows that $D_{Ni} \approx \chi_e$; the central region at low D_{Ni} and χ_e corresponds to the region below the critical threshold for turbulence in the electron temperature gradient.

In the case of MH, only the effective $\chi_{e,PB}$ from power balance, as obtained from an interpretative simulation by the JETTO code can be calculated, and the indication is that, as already found for the deuterium diffusivity, also $\chi_{e,PB}$ is about one order of magnitude higher than D_{Ni} in the plasma centre.

The analysis of discharges in L-mode (with ICRH in MC) confirms that also in this case the Ni diffusivity is quite similar to the deuterium and heat diffusivities [23]. An example is given in Fig.17 for the discharges shown in the previous sections. In both cases the Ni, deuterium and heat diffusivities are of the same order and have similar shapes. The central region at low diffusivity corresponds to the portion of the radius where the electron temperature gradient is below the critical threshold for turbulence, just as in the H-mode discharges with ICRH in MC discussed above. This transition in Ni, deuterium and heat transport occurs at the value of radius corresponding to a strong increase of the maximum growth rate of ITG/TEM instabilities, as estimated by the linear gyrokinetic code Kinezero [32].

6. GYROKINETIC CALCULATIONS

The linear version of the gyrokinetic code GS2 [21] has been applied in order to identify the unstable microinstabilities present in the JET plasmas considered in this paper as well as to study the transport of a nickel trace produced by such microinstabilities. At mid-radius, the main plasma parameters relevant for the stability of ITG and TEMs are, in the case of MH, $R/L_{Ti} = 6.6$, $R/L_{Te} = 4.0$, $R/L_n = 3.9$ and $T_e/T_i = 0.95$, whereas in the case of MC $R/L_{Ti} = 6.6$, $R/L_{Te} = 6.0$, $R/L_n = 5.2$ and $T_e/T_i = 1.0$. Here $R/L_x = -R\nabla_x/x$ is the normalized logarithmic gradient of the quantity x , R being the major radius of the plasma.

The results of the microstability analysis for plasmas with MH and MC are illustrated in Fig.19.

Calculations are electrostatic and effects of collisionality are taken into account for all the species by a pitch-angle scattering operator [21]. The growth rate and the real frequency of the most unstable mode as a function of the poloidal wave number $k_y \rho_i$ are plotted for Pulse No: 58144 with ICRH in MH (Fig. 19(a), (c) respectively) and for Pulse No: 58149 with ICRH in MC (Fig.19(b), (d)) .The growth rate has been divided by $k_{\perp} \rho_i^2$ averaged along the field line over the mode structure. The value of $k_y \rho_i$ for which $\gamma / \langle k_{\perp} \rho_i^2 \rangle$ is maximum identifies with good approximation the scale at which nonlinear transport is found to peak [33]. Such identification is important in order to establish the direction of propagation of the mode producing the largest amount of transport, which might be different from that of the mode with largest growth rate. In the MH discharge the dominant mode is an ITG, and the main drive is provided by the large value of R/L_{Ti} . These modes propagate in the direction of the ion diamagnetic frequency, namely the real frequency is positive. Instead in the case of MC the large value of R/L_n is above the threshold of the R/L_n driven TEM, and this is found to be the most unstable mode. The frequency is negative, namely the mode propagates in the electron diamagnetic direction.

The logarithmic density gradient is not the only parameter which increases when moving from MH to MC. A large variation is measured as well for R/L_{Te} , which increases from 4 to 6. Such a variation in R/L_{Te} is not large enough however to imply a change of the most unstable mode from ITG to TEM when moving from MH to MC. This is also confirmed by the fact that the frequencies of these modes increase with increasing wave number k_y , differently from what is expected for a R/L_{Te} driven TEM, for which the frequency of the mode decreases (propagates faster in the electron diamagnetic direction) with increasing k_y , namely going towards smaller scales. .

It is found that the heat transport produced by these dominant modes does not match the ratio electron to ion heat flux of the experiments. For instance, considering the experimental heat fluxes shown in Fig.2, around mid-radius the ratio ion to electron heat flux Q_i/Q_e is rather close to 1 in the MC heating scheme, while the most unstable mode provides a ratio Q_i/Q_e above 2. Such a disagreement can be reduced by assuming that also subdominant modes contribute to the total transport. These are not taken into account directly in these results, since the linear version of the GS2 code solves the linearised gyrokinetic equation by time integration and identifies only the fastest growing mode. However the existence of subdominant modes for these JET plasmas is confirmed by results obtained with fluid spectral codes, like the Multi-Mode (Weiland) Model [34] and the GLF23 model [35]. The value $R/L_{Te} = 6$ in the MC case is found to destabilize a R/L_{Te} driven TEM, which is instead almost stable in the case of MH, for which $R/L_{Te} = 4$.

The effects of these instabilities on the impurity transport are studied by including in the gyrokinetic calculations a trace of nickel. Calculations are electrostatic and include the effect of collisions on all the species.

The pairs of parameters $[R/L_n, R/L_{Te}]$, $[R/L_n, Te/Ti]$ and $[R/L_n, R/L_{Ti}]$ have been scanned over intervals largely covering the experimental variations in the considered discharges. For each set of parameters, the value of the normalized nickel logarithmic density gradient R/L_{nNi} has been varied

over the three values 0, 3 and 6. Particle transport has been computed with the quasi-linear model detailed in [36]. A linear dependence has been found between the Ni flux and the Ni logarithmic density gradient. Due to the fact that nickel is a trace in the plasma, a linear dependence between the Ni flux and the Ni logarithmic density gradient exists, allowing the unambiguous determination of D and v for nickel. The ratio $(-v/D)_{\text{Ni}}$, that in the limit of negligible sources determines the nickel density profile, has then been computed for the full set of input parameters described above.

Figure 20 shows the dependence of the Ni peaking factor $-R(v/D)$ on T_e/T_i and on R/L_{Te} at different values of R/L_n (from 1 to 6). A strong dependence on the logarithmic density gradient of the main species is found: by increasing R/L_n , the ratio $(-v/D)_{\text{Ni}}$ decreases, i.e. increasing density peaking corresponds to decreasing nickel peaking. It has to be observed that this effect is opposite to the usual behaviour of the neoclassical pinch velocity to diffusion ratio. Up to moderately peaked density profiles ($R/L_n = 4$) the impurity profiles become less peaked with increasing R/L_{Te} . Also the increase of the electron to ion temperature ratio has a flattening effect on the nickel profiles: large T_e/T_i values imply flat nickel profiles for any R/L_n . In Fig.20 the regions of the plasma parameters corresponding to the analysed JET discharges (MC and MH) is marked showing that, despite the low variations of the electron temperature and density profiles, the experimental findings are in qualitative agreement with these scalings.

In all these parameter scans, the most unstable modes are found to be ITGs or R/L_n driven TEMs.

In all conditions, the Ni pinch is found to be inwards, differently from the experimental findings. In order to investigate possible effects of subdominant modes driven by electron temperature gradients in these plasmas a parameter scan of the pair of parameters $[R/L_{Te}, R/L_{Ti}]$ has been done considering a fixed value of $R/L_n = 2$, namely below the threshold of the R/L_n driven TEM, which in these conditions is around 4.5. Results are illustrated in Fig.21. It is found that for small R/L_{Ti} and large R/L_{Te} values, a TEM driven by R/L_{Te} is the dominant mode, as shown by the change of sign of the real frequency. This mode produces a Ni pinch directed outwards. Such a reversal of the direction of the impurity pinch, connected with a transition from ITG to TEM, and with the corresponding reversal of the frequency of the mode, is found to be caused by impurity density fluctuations arising from the compression of parallel velocity fluctuations generated by the parallel electric force in the presence of a fluctuating potential [37]. Such a mechanism provides a contribution to the total impurity pinch, which is directed inwards for instabilities rotating in the ion diamagnetic direction, and outwards for instabilities rotating in the electron diamagnetic direction. Moreover it remains finite for increasing impurity charge and mass. In particular, the instability drive provided by a strong electron logarithmic temperature gradient is found to produce a total impurity pinch directed outwards, as shown by the results of Fig.21.

It has to be mentioned that effects of thermodiffusion due to the presence of a finite temperature gradient of the impurity trace cannot be used to explain such a transition, since they occur in the opposite direction for an impurity, namely an inward pinch for a TEM and an outward pinch for ITG [37,38,39]. Moreover, they decrease with increasing charge of the impurity and become

practically negligible for nickel [37].

Summarizing, a possible theoretical explanation of the Ni experimental behaviour is that in the case of MH, the transport is mainly generated by an ITG mode, while the value of $R/L_{Te} = 4$, when considered alone as in the case of small R/L_{Ti} shown in Fig. 21, is found to lead to instabilities characterized by very small growth rates and rather elongated along the field line, therefore producing very small transport. The impurity pinch is consistently observed directed inwards. On the contrary, in the case of MC, besides the R/L_{Ti} driven ITG or the R/L_n driven TEM, both producing an inward Ni pinch, the larger value of $R/L_{Te} = 6$ drives an unstable mode which, although subdominant, produces an additional contribution to the total impurity pinch which is directed outwards. This opens the possibility of a total pinch being small or outwards in these conditions, as observed in the experiments.

CONCLUSION

The analysis of the behaviour of nickel injected by LBO pulses in JET H-mode low collisionality discharges has shown that when ICRH is applied in ^3He Minority Heating to heat thermal ions very peaked Ni profiles are observed, while in discharges with ICRH applied in Mode Conversion to heat electrons Ni density profiles are slightly hollow or flat. The information available is not enough to discriminate whether the different effect of the two heating modalities can be ascribed to the different heating channel or to the difference in the power deposition profile or even to a combination of both. In any case, simulations by means of an impurity transport code have shown that this different behaviour corresponds to different transport parameters: in the MH discharges the diffusion coefficient in the plasma centre is low, close to the neoclassical value, and the pinch velocity is inward throughout the radius, with maximum values of about 3 m/s around $\rho = 0.4$. Instead, when ICRH is applied according to the MC scheme, the central Ni diffusivity is higher than the neoclassical one and the pinch velocity is slightly outward or zero.

In L-mode discharges, due to the presence of a significant sawtooth activity during LBO pulses in MH discharges, the simulation of the spectroscopic data has been made only for MC discharges. However, the comparison of the experimental SXR emissivity profiles (outside sawteeth) has shown a stronger peaking in MH discharges, similarly to what found in H-mode, even if in this case an inward pinch for Ni has been found also with ICRH in MC. In absence of detailed GS2 simulations, the linear code KINEZERO has been applied to these discharges, showing that in the region above the turbulence threshold in these L-mode discharges ITGs are always the most unstable modes.

In H-mode discharges the deuterium and heat diffusivity are found to be higher than the Ni one by one order of magnitude in the plasma centre when ICRH is applied in MH, while in the MC discharges the higher on-axis diffusivity found for nickel is of the same order of the deuterium and heat diffusivities, and the pinch velocity is quite lower, outward or close to zero. In both cases a region of high gradients for the diffusion coefficient has been found around $\rho = 0.3$, where also the pinch velocities show the highest difference. These results are in qualitative agreement with what already found in AUG [12], where in higher collisionality shots ECRH has been found to have a

greater effect than ICRH in increasing the central impurity diffusion coefficient, thus flattening the impurity density profiles. However, in [12] it is underlined that both ECRH and ICRH are effective in increasing the diffusivity when they are centrally applied, while in these JET discharges when ICRH is applied in MH the power deposition profiles are centrally peaked, but the diffusion coefficient is about neoclassical in the plasma centre.

By applying the linear version of the gyrokinetic code GS2, an interpretation in terms of the theory of ITG and TEMs has evidenced a qualitative agreement between theory and observations in the scaling of the impurity peaking with the plasma logarithmic gradients. In particular, a mechanism of particle pinch whose direction matches the pinch reversal observed in the experiments when moving from MH to MC conditions has been identified in the effect arising from the compression of parallel velocity fluctuations. This leads to a pinch contribution whose direction reverses from inwards to outwards when the dominant mode changes from ITG to TEM and correspondently its direction of propagation moves from the ion diamagnetic to the electron diamagnetic direction. Such a contribution becomes strong in the presence of large logarithmic electron temperature gradients, resulting in total particle pinches directed outwards. In qualitative agreement, in the experiments it is found that the parameter R/L_{Te} in plasmas heated by MC, in which the Ni pinch is small and outwards, is significantly larger than in the case of MH plasmas, in which the impurity pinch is larger and inwards. Such an explanation, obtained by the present quasi-linear analysis, should be considered as a first indication of a possible agreement between theoretical predictions and experimental observations: more conclusive results need fully comprehensive non-linear gyrokinetic simulations. In particular the effect of the simultaneous presence of different modes cannot be computed properly within such a quasi-linear treatment, and the simple assumption that the total transport is given by a summation over the transport produced by all unstable modes might be inadequate. Nonlinear simulations however go certainly beyond the purpose of the present work, and are left for a separate and specific theoretical future study.

Concerning the relationship between particle and heat transport, in L-mode $D_{Ni} \sim \chi_e$ and also nickel and deuterium have similar diffusion in the plasma core; D_{Ni} profiles are well correlated with the profiles of electron temperature inverse gradient length, showing transition from low to high transport when the critical value found for electron heat is exceeded.

The results discussed in this paper confirm that the heating channel and the power deposition profile may be an important tool to control the impurity behaviour also at ITER relevant collisionalities, specifically through the excitation of TEM modes.

Although a scaling of the Ni behaviour with collisionality and applied power cannot be provided, the results found in these discharges at ITER relevant collisionality suggest that it should be possible in ITER to find conditions in which the accumulation of impurities such as nickel can be contained.

ACKNOWLEDGMENTS

The authors are grateful to Dr. L. Zabeo for the inversions of the interferometer data

REFERENCES

- [1]. Angioni C. et al., Phys. Rev. Lett. **90** (2003) 205003
- [2]. Weisen H., et al., Nucl. Fusion **45** (2005) L1-L4
- [3]. Peeters A. G., et al., Nucl. Fusion **45** (2005) 1140
- [4]. Angioni C. et al., Nucl. Fus. **44** (2004) 827
- [5]. Angioni C. et al., Phys. Plasmas **12** (2005) 040701
- [6]. Stober J. et al., Nucl. Fusion **43** (2003) 1265
- [7]. Weisen H., Furno I. and TCV Team, Nucl. Fusion **41** (2001) 1227
- [8]. Ernst D. et al., Phys. Plasmas **11** (2004) 2637
- [9]. Angioni C., Peeters A.G., Jenko F., Dannert T., Phys. Plasmas **12** , 112310 (2005).
- [10]. Romanelli M., Bourdelle C., Dorland W., Phys. of Plasmas **11** (2004) 3845
- [11]. Neu R. et al., Plasma Phys. Control. Fusion **44** (2002) 811
- [12]. Dux R, et al., Plasma Phys. Control. Fusion **45** (2003) 1815
- [13]. Gohil P., et al., Plasma Phys. Control. Fusion **45** (2003) 601
- [14]. Takenaga H., et al., Nucl. Fusion **43** (2003) 1235
- [15]. Marmar E.S. et al. , Nucl. fusion **43** (2003) 1610
- [16]. Puiatti M.E., et al. , Plasma Phys. Control. Fusion **45** (2003) 2011
- [17]. Nave M.F.F. et al. , Nucl. Fusion **43** (2003) 1204
- [18]. Scavino E, Bakos J, Weisen H, Plasma Phys. Control. Fusion **46** (2004) 857
- [19]. Rice J.E. et al. , Nucl. Fusion **42** (2002) 510
- [20]. Mantsinen M., et al., Proc. 28th EPS Conf. on Plasma Physics and Controlled Fusion, Funchal, Portugal, (2001) Vol. ECA25A , 1745
- [21]. Kotschenreuther M. et al. , Comput. Phys. Commun. **88** (1995) 128
- [22]. Mantica P. et al., proc. 19th IAEA Conf. Lyon, France, (2002), EX/P1-04
- [23]. Mantica P., et al., Proc. 30th EPS Conf. on Plasma Physics and Controlled Fusion, St Petersburg, Russia (2003), vol ECA27A, O3.1A
- [24]. Garzotti L., et al., Nucl. Fusion **43** (2003) 1829
- [25]. Mattioli M. et al., J. Phys. B: At .Mol. Opt. Phys. **34** (2001) 127
- [26]. Mattioli M. et al. , J. Phys. B At .Mol. Opt. Phys. **37** (2004) 13
- [27]. Houlberg W.A. et. al., Phys. of Plasmas, **4** (1997) 3230
- [28]. Challis C.D. et al., Nucl. Fusion **29** (1989) 563
- [29]. Eriksson L.G, Hellsten T., Will'en U. nucl. Fusion **33** (1993) 1037
- [30]. Garbet X. et al., Plasma Phys. Control. Fusion **46** (2004) 1351
- [31]. Puiatti, M.E. et al., Proc. 31st EPS Conf. on Plasma Physics and Controlled Fusion, London , (2004) ECA Vol. 28C, P1.151
- [32]. Bourdelle C., et al., Nucl. Fusion **42** (2002) 892
- [33]. Jenko F., Dannert T, Angioni C., Plasma Phys. Control. Fusion **47** (2005) B195
- [34]. Bateman G., Kritz A.H., Kinsey J.E., Redd A.J., Weiland J., Phys. Plasmas **5**, 1793 (1998).

- [35]. Waltz R. E., et al., Phys. Plasmas **4**, 2482 (1997).
 [36]. Angioni C., Peeters A.G., Jenko F., Dannert T., Phys. Plasmas **12**, 112310 (2005).
 [37]. Angioni C., Peeters A.G., submitted to Phys. Rev. Letters
 [38]. Garbet X. et al., Phys. Rev. Lett. **91** (2003) 035001
 [39]. Garbet X, Dubuit N. et al., Phys. of Plasmas **12** (2005) 082511-1

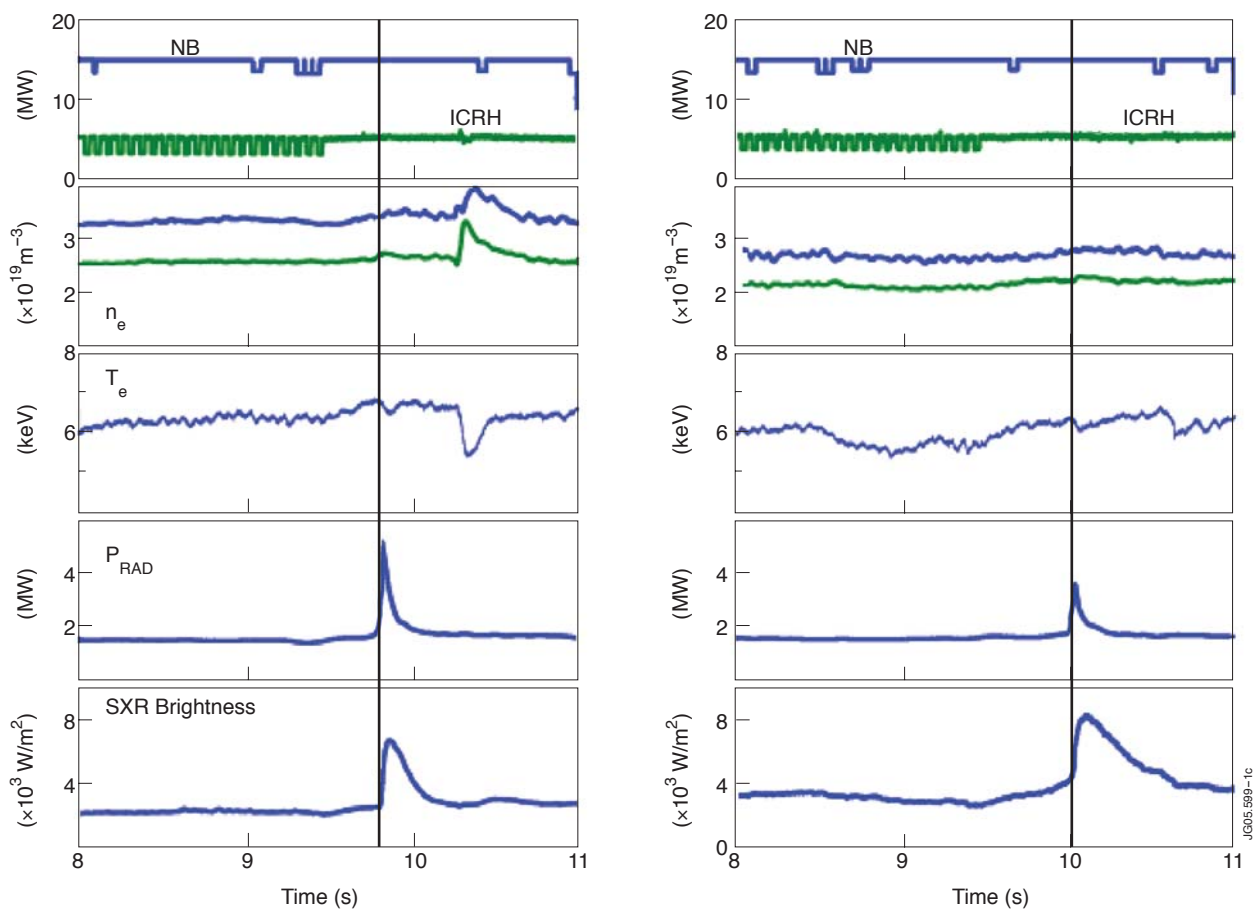


Figure 1: Time evolution of the main plasma parameters in the H-mode Pulse No: 58149 with ICRH in Mode Conversion (a) and Pulse No: 58144 with ICRH in Minority Heating (b). From top to bottom: neutral beam and ICRH heating power; electron density on axis and at $\rho = 0.4$ from SVD inversions of interferometer data; electron temperature from ECE; radiated power; soft X-rays brightness from a central line-of-sight.

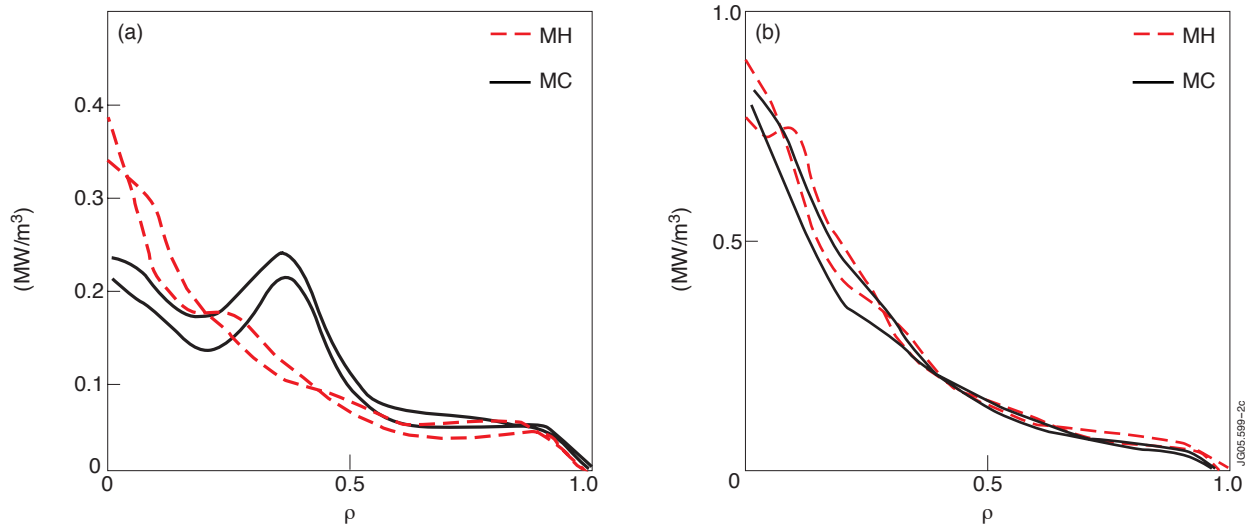


Figure 2: Electron (a) and ion (b) power deposition profiles in the H-mode discharges with ICRH in MC (solid line, Pulse No's: 58149 and 58143) and MH (dashed line, Pulse No's: 58142 and 58144)

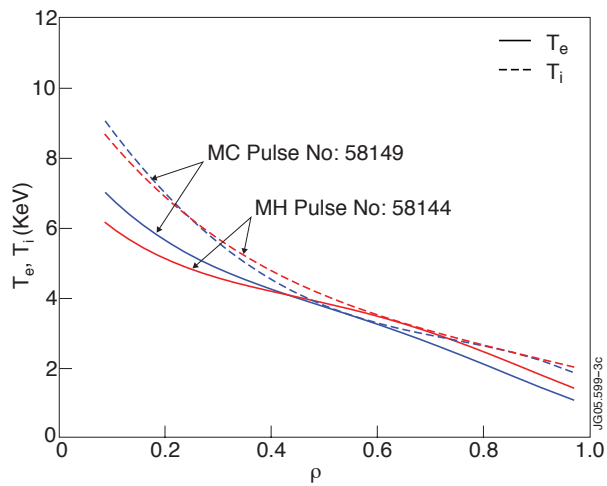


Figure 3: Ion and electron temperature profiles, in H-mode discharges with ICRH in MC (solid line, Pulse No: 58149) and in MH (dashed line, Pulse No: 58144). The ion temperature is from CXRS, the electron temperature is obtained as an average between ECE and Lidar Thomson scattering.

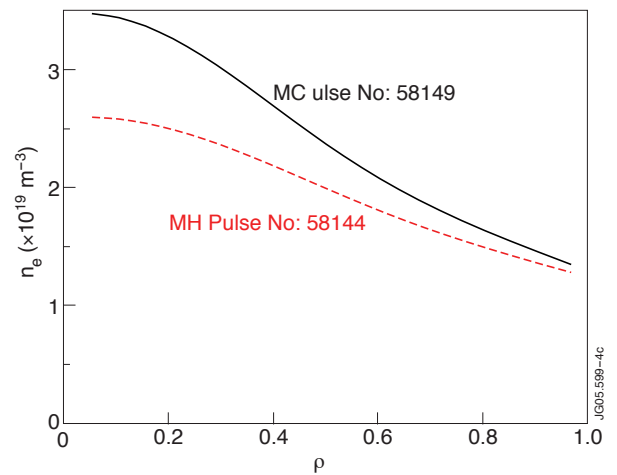


Figure 4: Electron density profiles in the H-mode discharges with ICRH in MC (Pulse No: 58149) and in MH (Pulse No: 58144), as obtained from SVD inversions of the interferometer data.

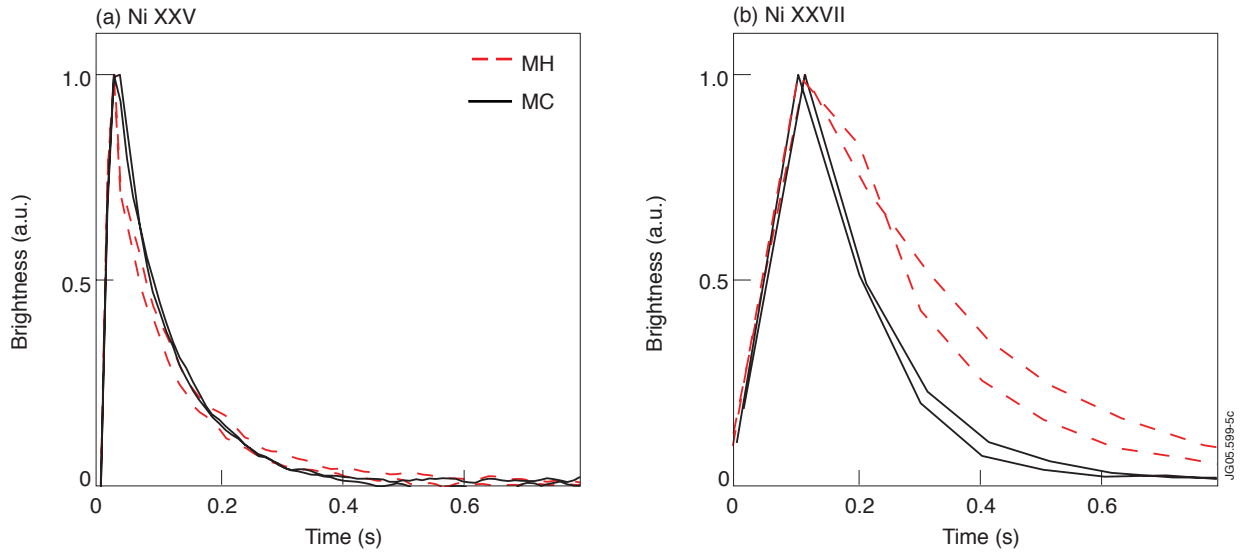


Figure 5: Experimental time evolution during the LBO pulse of the Ni XXV (a) and Ni XXVII (b) brightnesses in H-mode discharges with ICRH in MC (solid line, Pulse No's: 58149 and 58143) and in MH (dashed line, Pulse No's: 58142 and 58144). The signal before LBO has been subtracted.

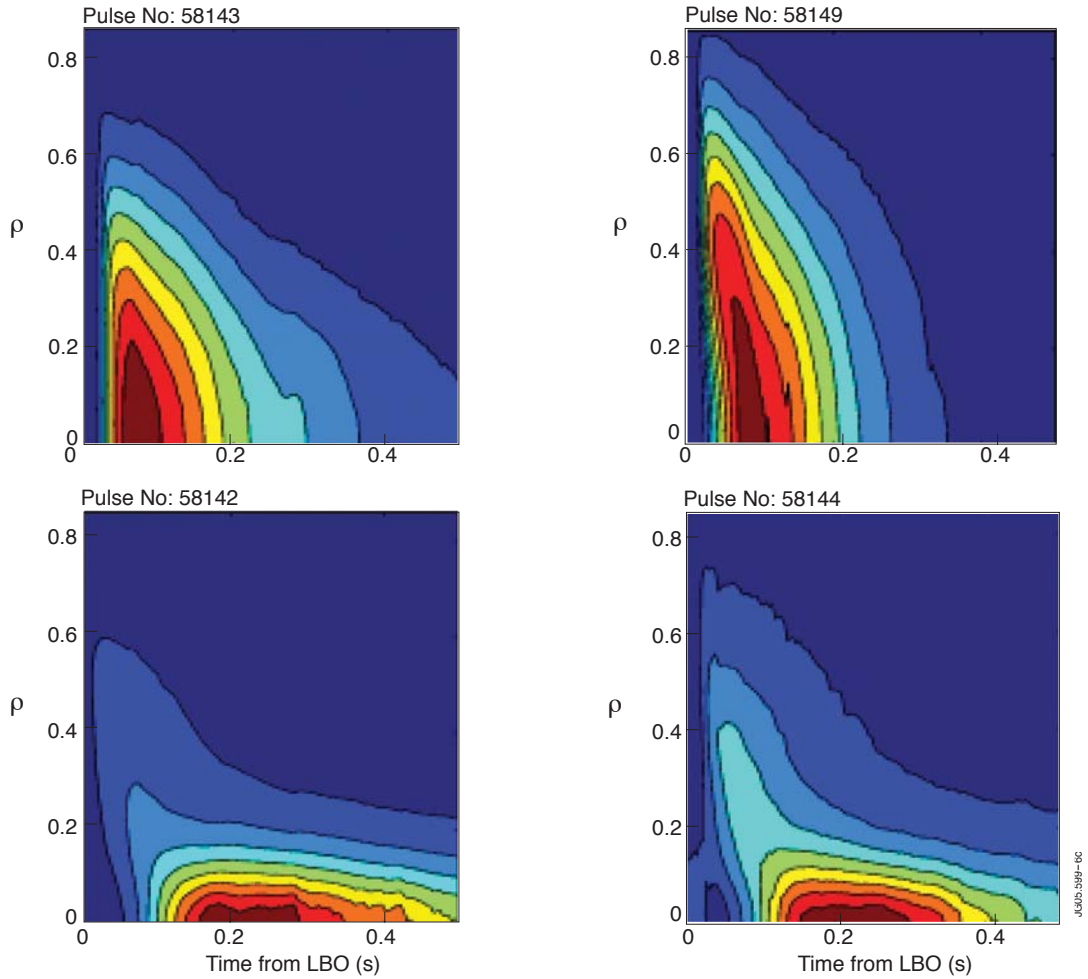


Figure 6: Contour plot of the inverted SXR emissivity with ICRH in MC and in MH (H-mode) during the LBO pulse. The emissivity before LBO has been subtracted.

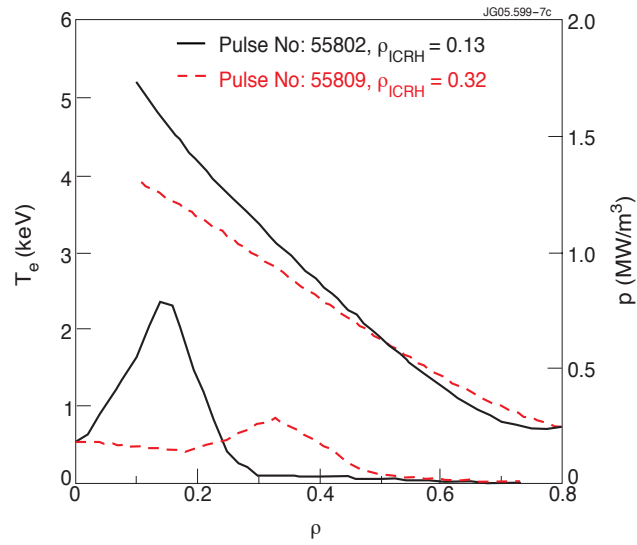


Figure 7: Electron temperature and electron power deposition profiles in L-mode discharges, with different deposition radius of ICRH (MC for both discharges)

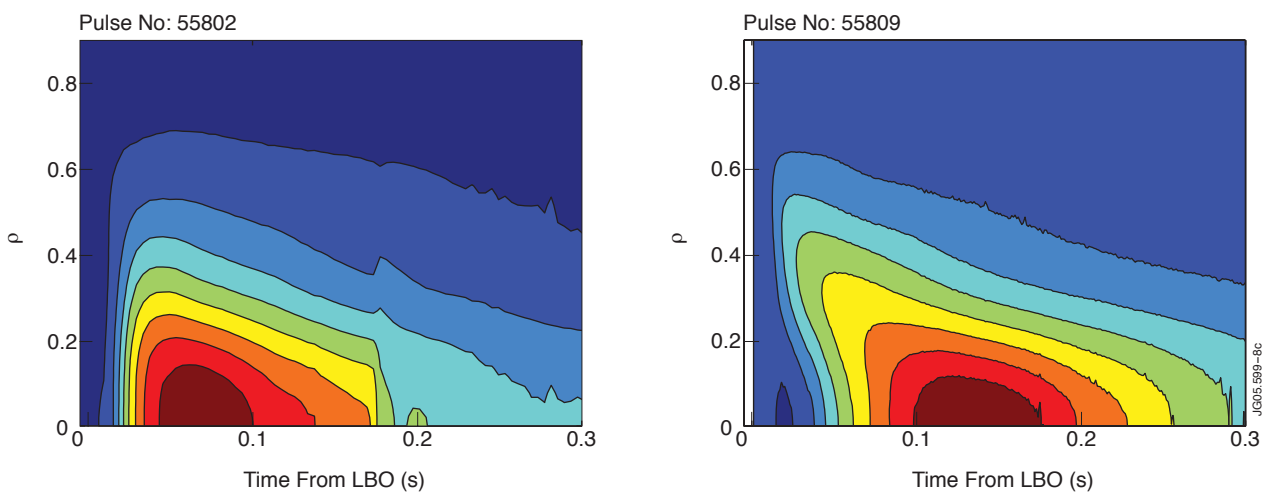


Figure 8: contour plot of the inverted SXR emissivities in two MC L-mode discharges with different ICRH deposition radii

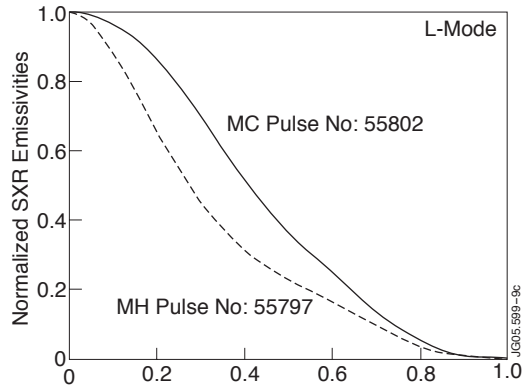


Figure 9: Normalized experimental SXR emissivity profiles in two L-mode discharges, one (Pulse No: 55802, solid line) with ICRH in MC, the other (Pulse No: 55797, dashed line) with ICRH in MH

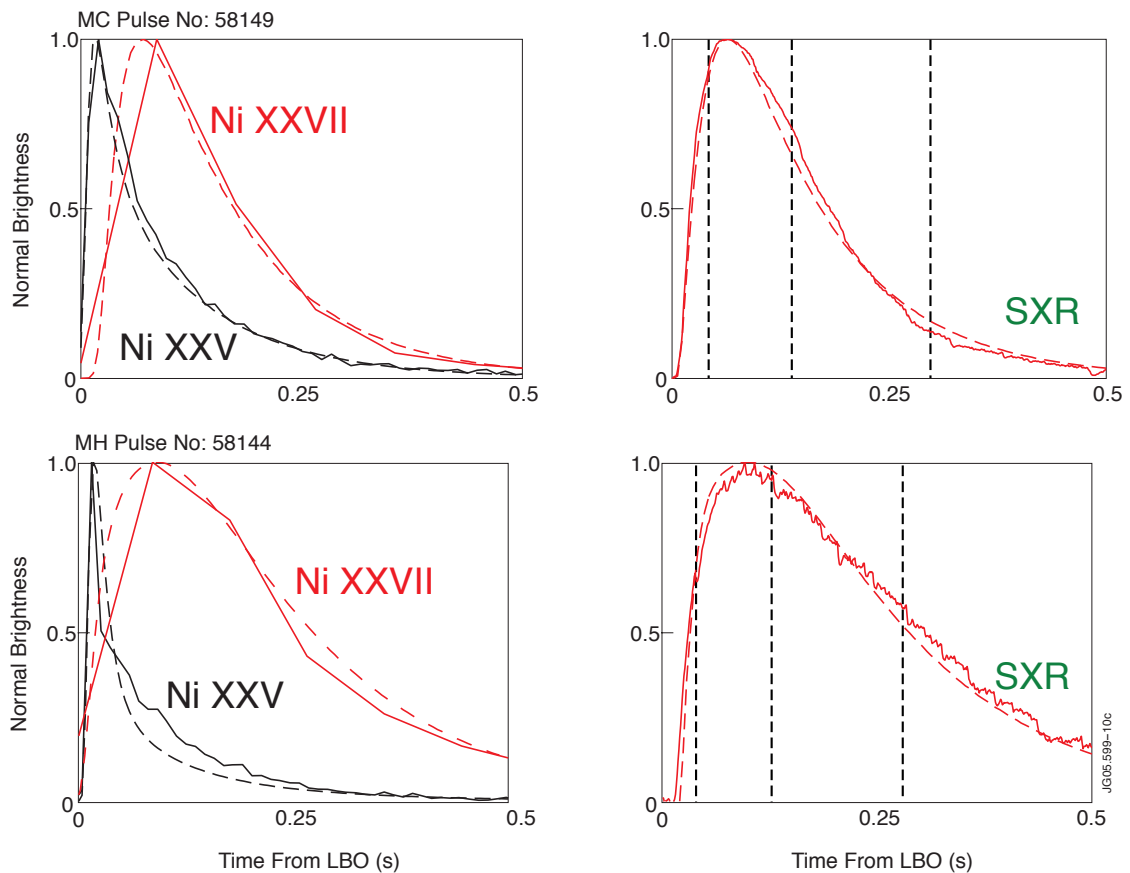


Figure 10: Time evolution of the experimental (solid lines) and simulated (dashed lines) brightnesses of Ni XXV and Ni XXVII lines and of soft X-rays during the LBO pulse in discharges with ICRH in MC (top) and in MH (bottom). The vertical lines on the left plot correspond to three times at which the simulated and experimental SXR profiles are compared in Fig. 11.

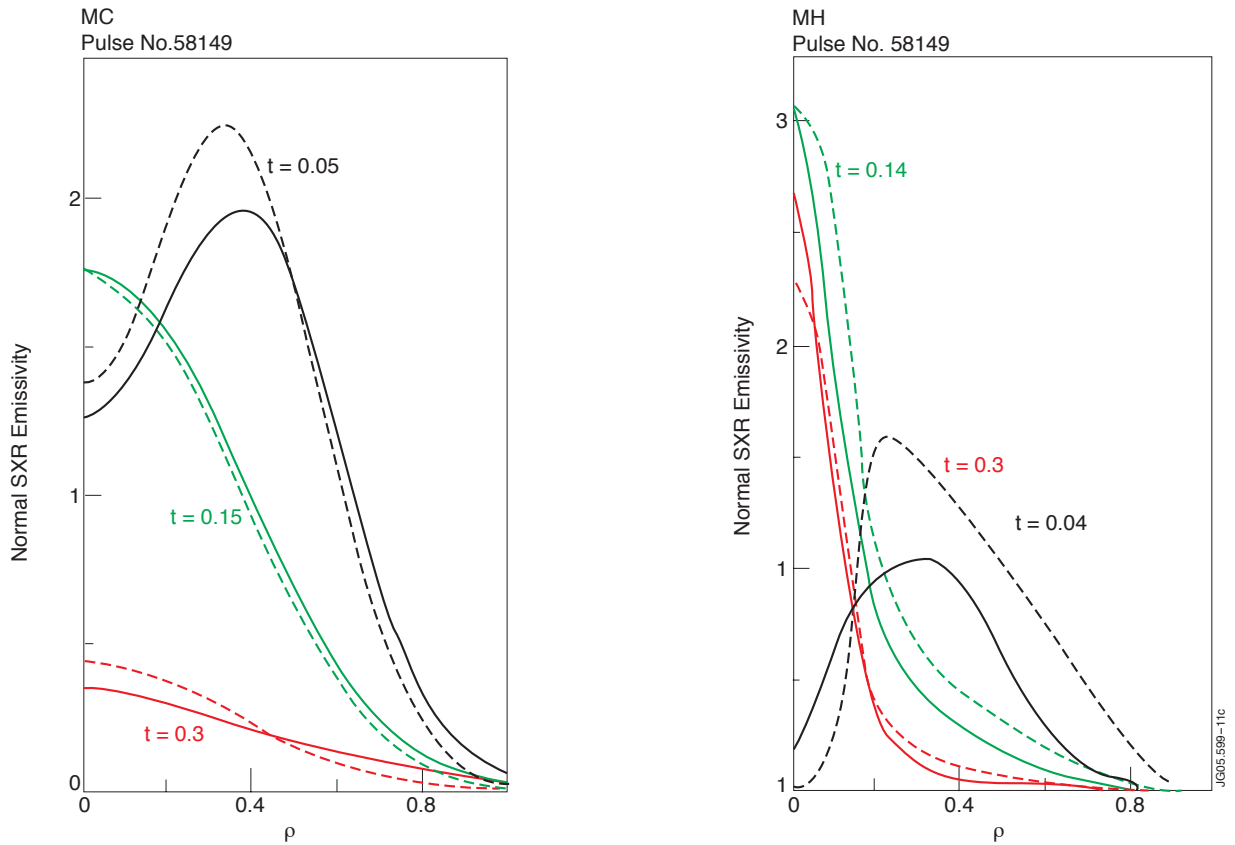


Figure 11: Experimental (solid lines) and simulated (dashed lines) SXR emissivity profiles at three times, the first during the Ni penetration phase, the second around the maximum of the emission and the last one during the decay phase (see vertical lines in fig. 10).

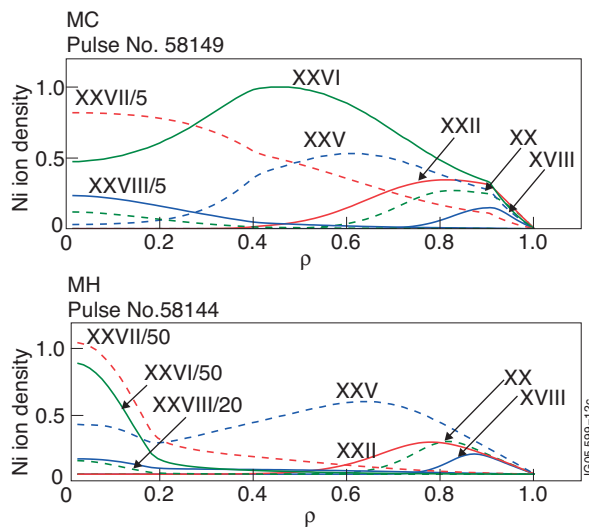


Figure 12 Normalized Ni ion density profiles in two H-mode discharges, #58149 with ICRH in MC and #58144 with ICRH in MH.

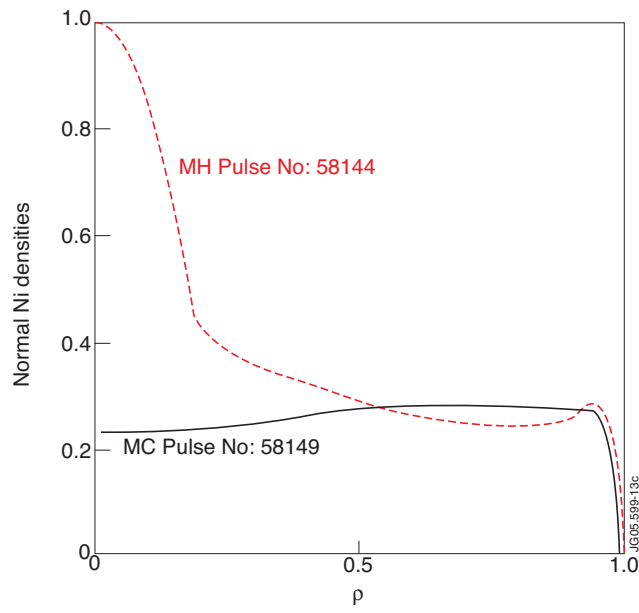


Figure 13: Comparison of total Ni density profiles as obtained from an extrapolation of the simulation to the steady state for discharges with ICRH in MC and in MH.

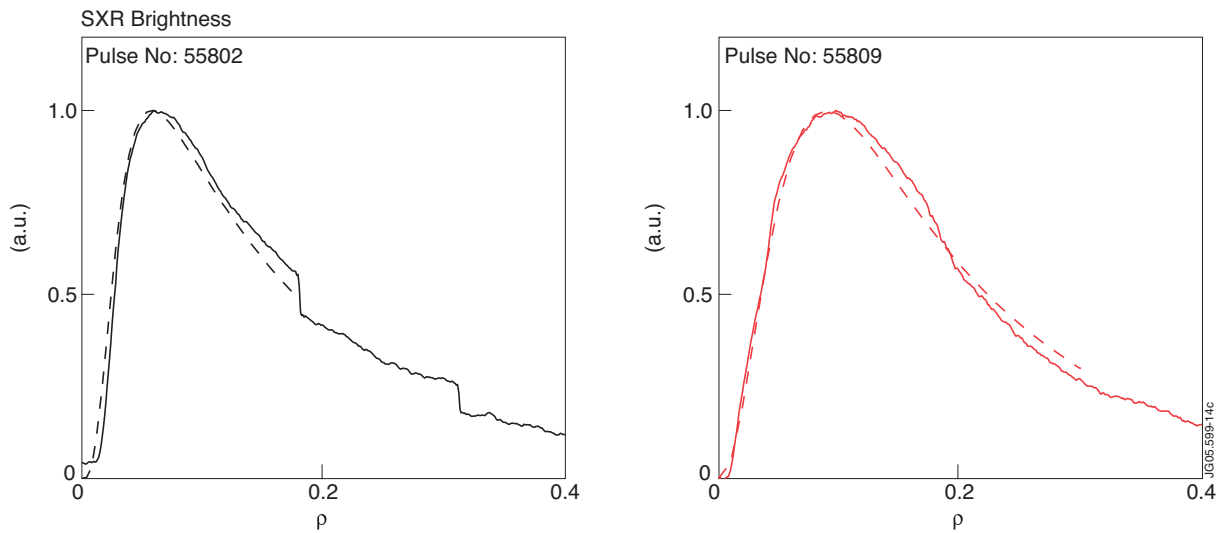


Figure 14 : Time evolution of the experimental (solid lines) and simulated (dashed lines) SXR brightnesses along a central chord in two L-mode discharges, one (Pulse No: 55802 ,left) with ICRH deposition radius at $\rho = 0.13$, the other (Pulse No: 55809, right) with ICRH deposition radius at $\rho = 0.32$

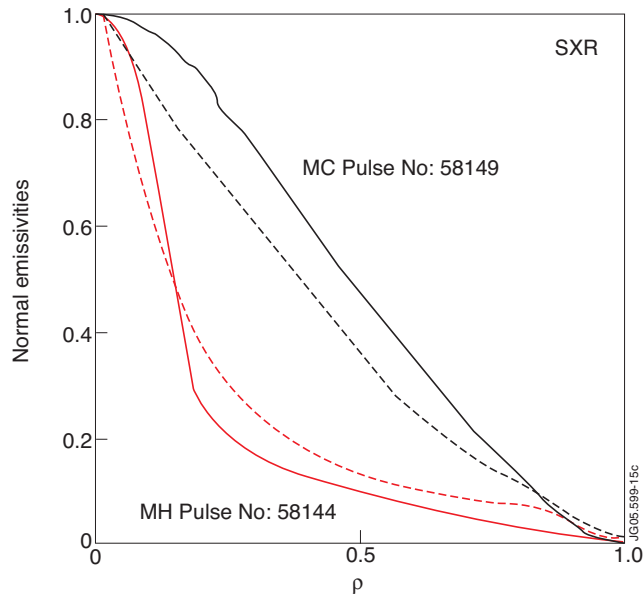


Figure 15: Comparison between the SXR emissivity profiles obtained by extrapolating the simulation to the steady state and the experimental SXR emissivity profiles outside the LBO pulse. In the two H-mode discharges, one with ICRH in MC, the other with ICRH in MH

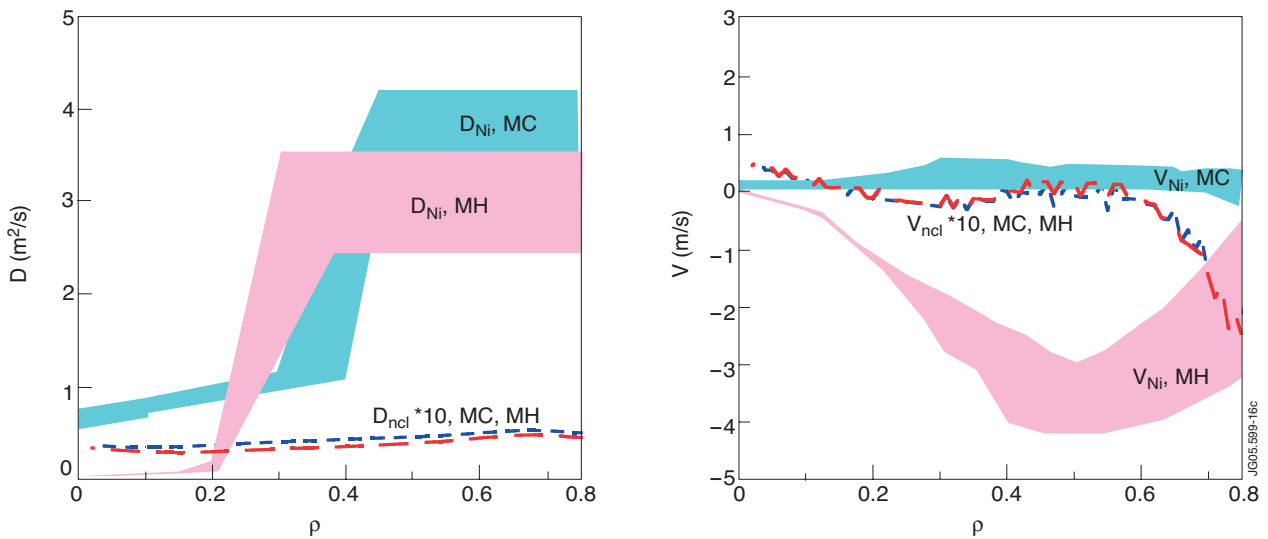


Figure 16: Diffusion coefficients (left) and pinch velocities (right) obtained by the simulations for Pulse No's: 58149 with ICRH in MC and 58144 with ICRH in MH. The colored area covers the values of D and v obtained with various runs minimizing the difference between the calculated and experimental radiation pattern. The neoclassical transport parameters are also shown.

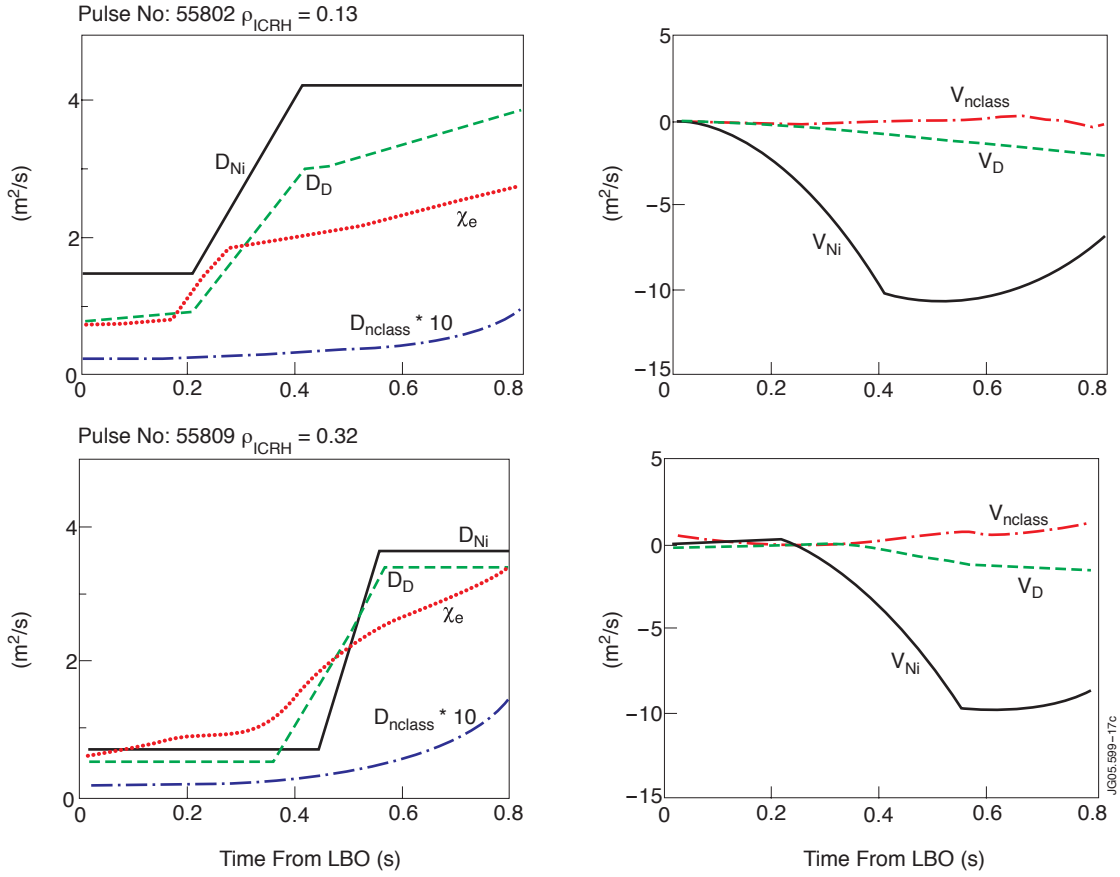


Figure 17: Left: comparison between Ni (solid line), deuterium (dashed line), neoclassical (dot-dashed line) and heat turbulent (dotted line) diffusivities in the two L-mode Pulse No's: 55802 and 55809 with different ICRH deposition radii. Right: comparison between Ni (solid line), deuterium (dashed line) and Ni neoclassical (dot-dashed line) pinch velocities in the same discharges

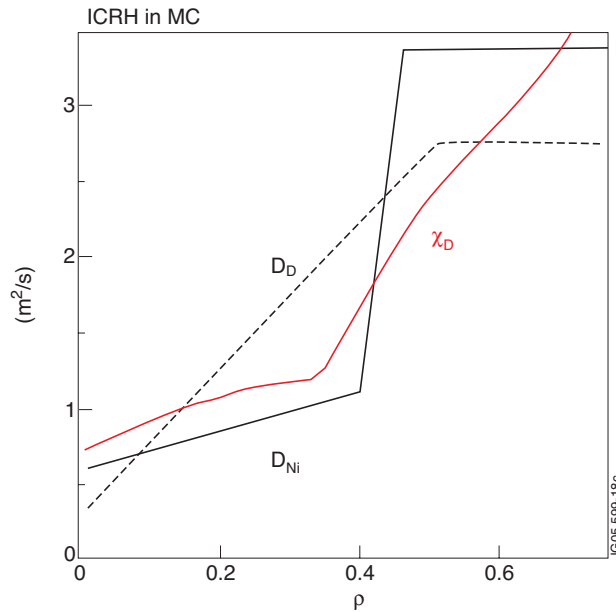


Figure 18: Comparison between the Ni diffusion coefficient obtained from the best simulation of the spectroscopic data (solid blue line) and the deuterium (dashed) and turbulent heat (green line) diffusivities in the H-mode discharge with ICRH in MC.

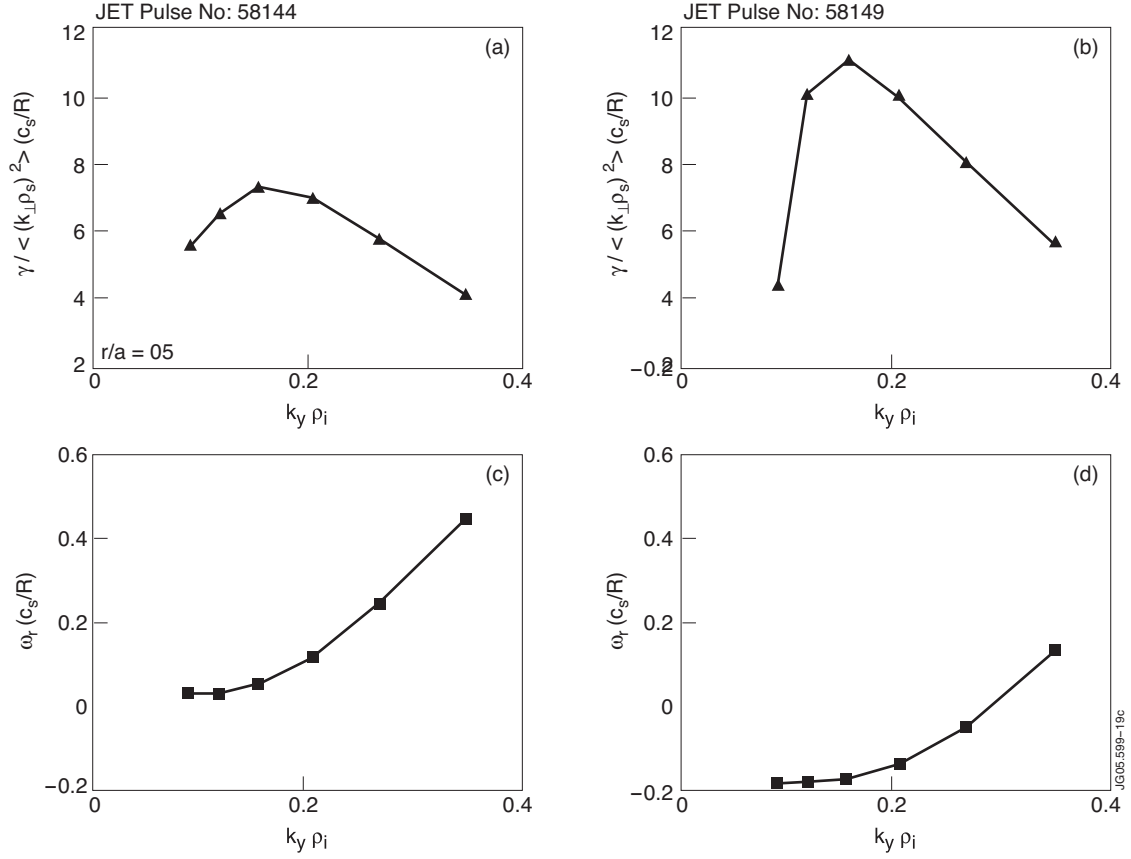


Figure 19: GS2 calculations of the growth rate (a, b) and real frequency (c, d) of the most unstable linear mode as a function of the poloidal wave number $k_y \rho_i$ calculated for two H-mode discharges with ICRH in MH (a, c) and MC (b, d). Frequencies are normalized to c_s/R , where $c_s = (T_e/m_i)^{1/2}$ is the sound speed and R is the plasma major radius

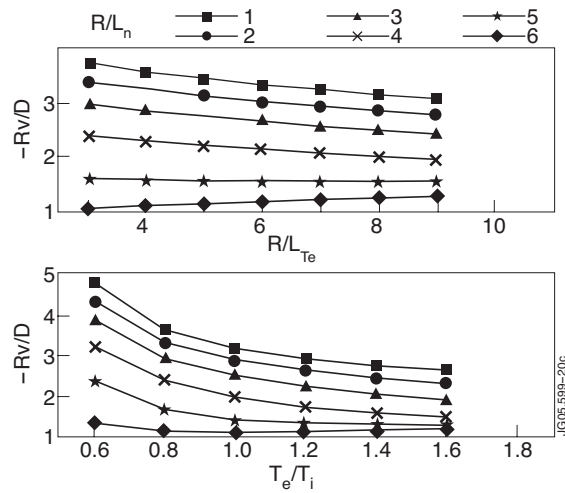


Figure 20: Nickel peaking factor $-Rv/D$ as a function of the normalized temperature gradient (top) and of the electron to ion temperature ratio (bottom) as obtained by the gyrokinetic code GS2 for 6 values of the logarithmic density gradient, from 1 to 6, accordingly to the legend box.

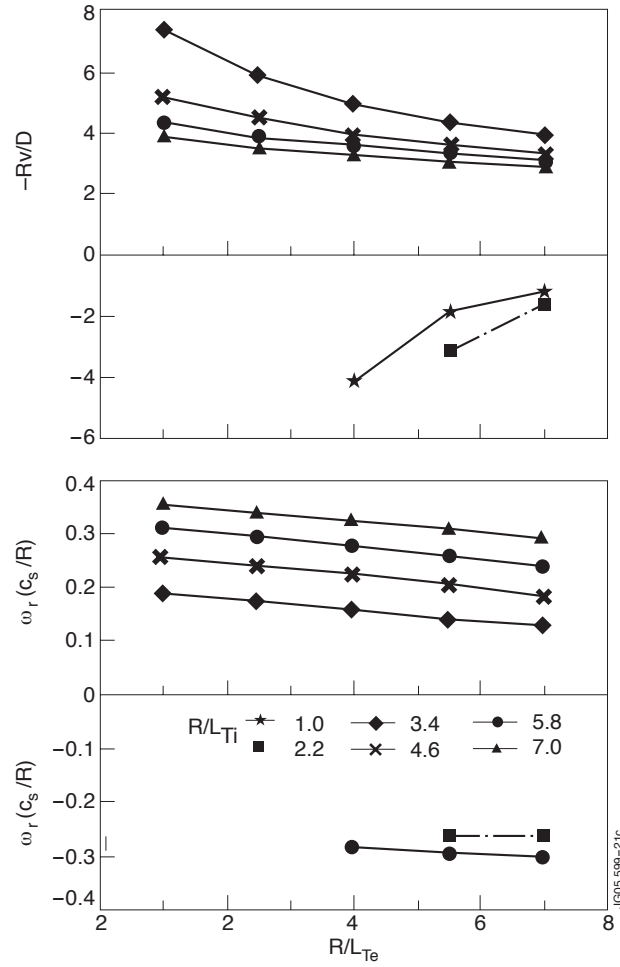


Figure 21: GS2 calculations of the Ni peaking factor $-Rv/D$ (top) and real frequency of the most unstable mode (bottom) as a function of the logarithmic electron temperature gradient R/L_{Te} for 6 values of the logarithmic ion temperature gradient R/L_{Ti} , with fixed $R/L_n=2$.